JOURNAL OF GEOPHYSICAL RESEARCH, VOL. 87, NO. B2, PAGES 927–935, FEBRUARY 10, 1982

# Application of Wave Field Continuation to the Inversion of Refraction Data

GEORGE A. MCMECHAN

*Pacific Geoscience Centre, Earth Physics Branch, British Columbia V8L 4B2, Canada*

ROBERT W. CLAYTON[1]

*Department of Geophysics, Stanford University, Stanford, California 94305*

WALTER D. MOONEY

*U. S. Geological Survey, Menlo Park, California 94025*

Three examples of the inversion of refraction data by downward continuation illustrate the applicability of the method to field data. The first example is a refraction profile from the Mojave Desert, California. These data are spatially aliased and contain clear evidence of lateral inhomogeneity. The inversion in this case produces a broken image in the slowness-depth domain due to the lateral inhomogeneity, but a useful average velocity model is still obtained. The second example is a shallow marine reflection profile. Here, the truncation effects due to the finite horizontal aperture of the recording cable produce artifacts in the slowness-depth domain. The velocity model is, however, distinct from these artifacts, and the presence of strong precritical reflections aids in the inversion. The third example is another shallow marine reflection profile. The inversion of these data illustrate the utilization of constraints provided by multiples as well as primary arrivals.

## INTRODUCTION

Recently, a downward continuation method was presented for the inversion of densely recorded refraction data [*Clayton and McMechan*, 1981*a*, *b*]. This technique transforms the entire recorded data wavefield from the time-distance ($t$-$x$) domain into the slowness-depth ($p$-$z$) domain. The resulting velocity-depth locus is a focussed image in the $p$-$z$ domain, and the uncertainty in the solution is indicated by the width and coherence of this image. There are two basic assumptions in the procedure which limit its general applicability. The first is the assumption of lateral homogenity of the velocity structure, and the second is the assumption that the data are sufficiently well sampled in the spatial dimension so that they can be treated as a wave field.

In this paper we present three examples of the application of this method to real refraction data. The main object of the paper is to illustrate the technique when applied to data which do not rigidly satisfy the assumptions mentioned above. Before considering the data, a brief review of the inversion procedure is given.

The downward continuation method consists of two linear, reversible wave field transformations [*Clayton and McMechan*, 1981*a*]. The first transformation is a slant stack of the $t$-$x$ data [*Schultz and Claerbout*, 1978; *Chapman*, 1978, 1981; *McMechan and Ottolini*, 1980]:

$$S(\tau, p) = \int_{-\infty}^{+\infty} P(\tau + px, x)\, dx \qquad (1)$$

Here $P(t, x)$ is the observed (seismogram) wave field, $S(\tau, p)$ is the transformed wavefield, $p$ is the horizontal slowness, $\tau$ is the time intercept, $x$ is the shot-receiver distance, and $t(=\tau + px)$ is the travel time. Each point in the $\tau$-$p$ plane is obtained by performing the integration in (1) over all points in the $t$-$x$ data along a line of slope $p$ and time intercept $\tau$. This operation decomposes the data wave field into plane wave elements. (Strictly, the slant stack transformation is insufficient to generate the plane wave response for a point source [*Chapman*, 1981], but our results do not depend significantly on this interpretation of the $p$-$\tau$ wave field). The slant stack integral (1)

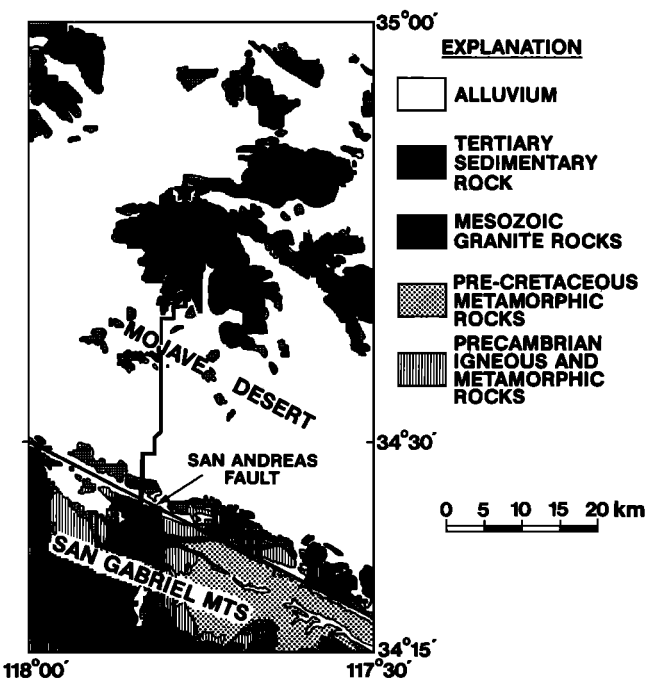


Fig. 1. Location of the Mojave Desert refraction profile. The star is the shot point. The recording instruments were placed along the line extending southward from the shot point. The seismograms recorded on this profile are shown in Figure 2.

[1] Now at Division of Geological and Planetary Sciences, California Institute of Technology, Pasadena, California 91125.



Paper number 1B1612.
0148-0227/82/001B-1612$01.00

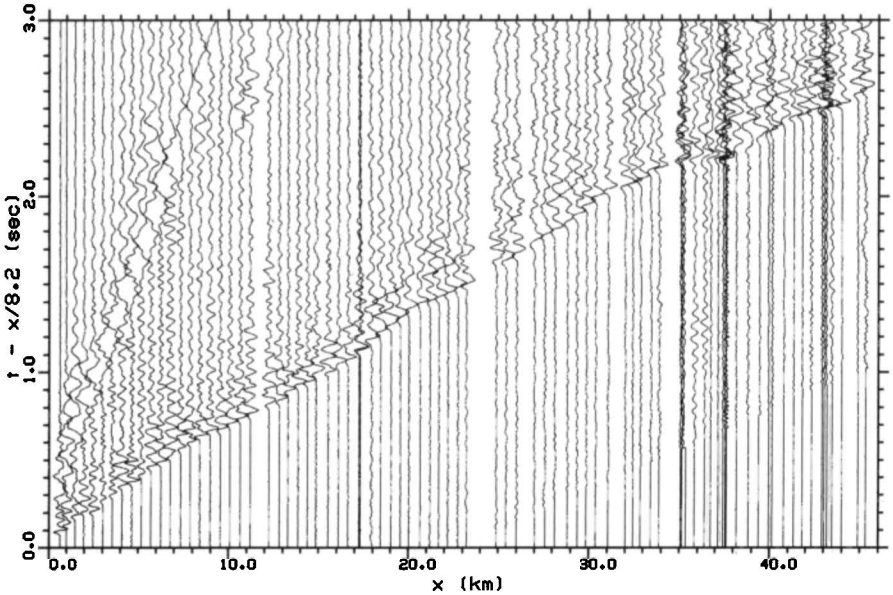


Fig. 2. Record section from the Mojave Desert data with a reduction velocity of 8.2 km/s. This profile is a composite of recordings of two shots, a smaller one recorded at $x < 10$ km and a larger one recorded at $x > 10$ km. The records are normalized so each has the same maximum amplitude.

produces a wave field in which the $p$-$\tau$ curve (the 'tau' curve of *Bessonova et al* [1974]) is imaged. This step is done only once. The slant stack itself may be viewed as a mathematical transformation which makes no physical assumptions about the nature of the field. However, to interpret $p$ as the horizontal slowness, it is necessary to assume lateral homogenity. Also, to produce a reasonable tau curve image, it is necessary that the data be sampled sufficiently densely in $x$ so as to avoid severe aliasing [*Brocher and Phinney*, 1981].

The second transformation is an iterative downward continuation of $S(\tau, p)$:

$$s(p, z) \equiv S(\tau = 0, p, z)$$

$$= \int S(\omega, p, z = 0) e^{-i\omega\Psi(p,z)}\, d\omega \qquad (2)$$

where

$$\Psi(p, z) = 2\int_0^z |v^{-2}(z) - p^2|^{1/2}\, dz$$

In (2), $s(p, z)$ is the solution wave field, $v(z)$ is velocity as a function of depth $z$, and $\omega$ is the temporal frequency. Implicit in (2) is the assumption of lateral homogenity of the velocity model because the up and downgoing raypaths are assumed to be identical. This transformation of $S(\tau, p)$ is repeated with successive modifications to $v(z)$ until the downward continued wavefield $s(p, z)$ images the input $v(z)$ function. This condition of stationarity indicates that convergence has been achieved (i.e., the $v(z)$ function that produces stationarity is the solution). A more detailed discussion is given by *Clayton and McMechan* [1981*a*].

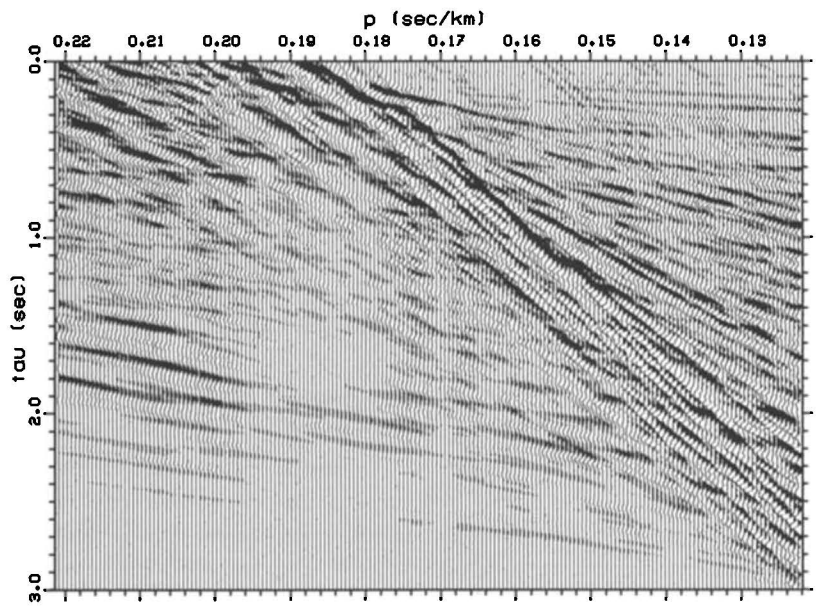


Fig. 3. Slant stack ($p$-$\tau$) wave field obtained by transformation of the Mojave Desert data in Figure 2 via equation (1). Iterative downward continuation of this wave field produces the velocity-depth model.

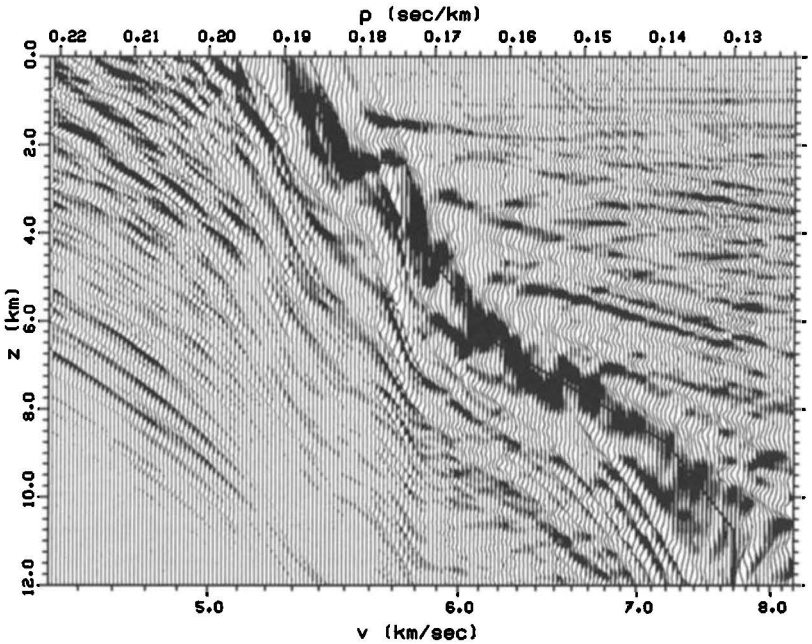


Fig. 4. The slowness-depth ($p$-$z$) wave field of the Mojave Desert data at convergence. The solid line superposed on the wave field is the velocity-depth model used in the final iteration in the downward continuation. The coincidence of the solid line and the image shows the convergence.

The main restrictions on the applicability of the downward continuation approach to inversion are that typical refraction data are spatially aliased and that the earth structure is often laterally inhomogeneous. In the sections that follow, realistic examples are considered that do not rigidly satisfy the assumptions of the method and hence serve to illustrate the robustness and utility of the wave field approach even when the data are not ideal. Three data sets are presented. The first profile is composed of vertical component velocity records from the Mojave Desert, and the other two are suites of acoustic responses recorded by hydrophone cables in shallow marine environments.

## The Mojave Desert Profile

In the fall of 1980, the U.S. Geological Survey conducted an extensive refraction project in the Mojave Desert of southern California. Only a portion of these data will be analyzed here. The location of the profile we have chosen is shown in Figure 1, and the data traces are shown in Figure 2.

A number of features are evident in the data (Figure 2). The first arrivals do not form a smooth locus of constantly decreasing slope ($p$), as would be observed if the earth structure were laterally homogeneous. Most of these fluctuations can be attributed to surficial sediments [*Fuis*, 1981]. Others, such as the

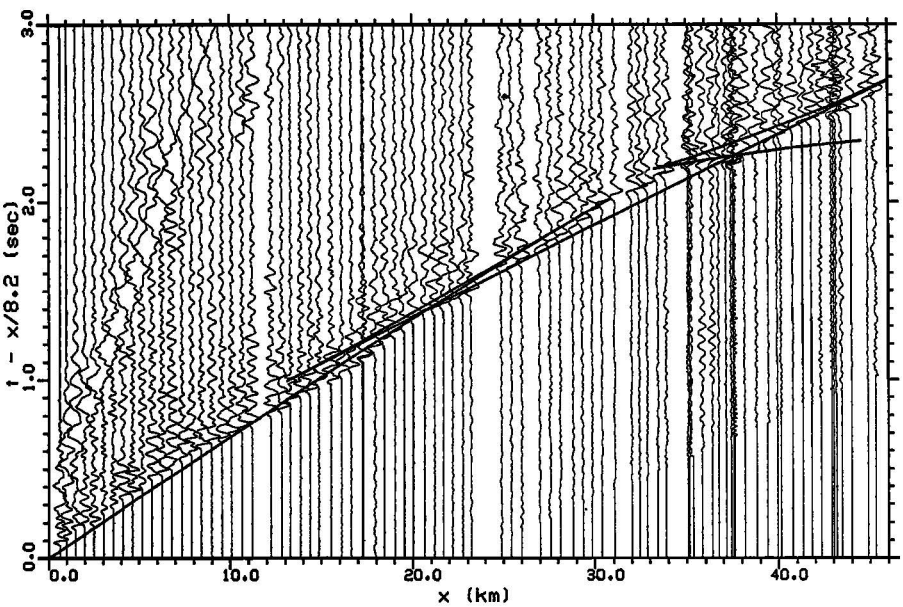


Fig. 5. Comparison of observed travel times with those computed for the velocity depth function shown as the solid line in Figure 4.

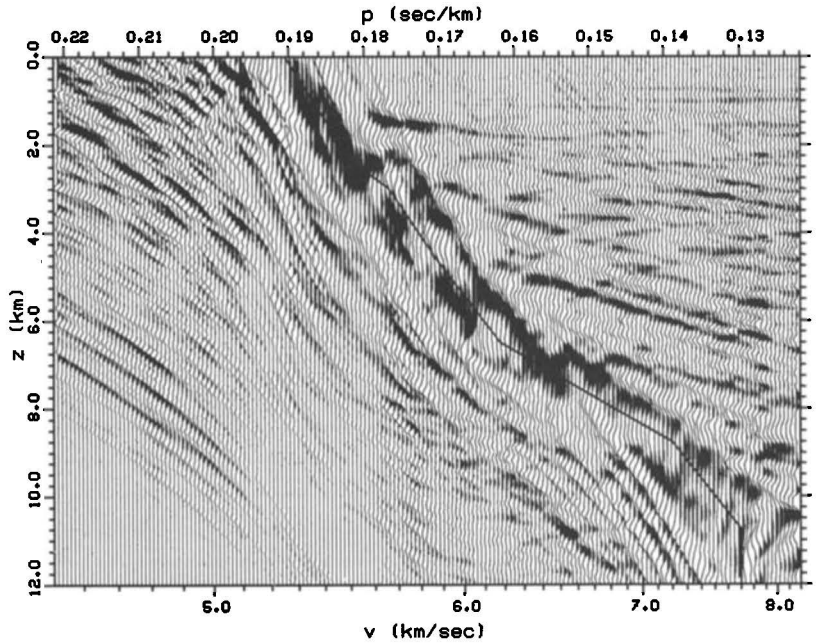


Fig. 6. An acceptable but unconverged downward continuation solution. The solid line is a velocity-depth curve that produces acceptable travel times (see Figure 7) but does not correspond to stationarity of the $p$-$z$ wave field.

early arrivals near $x = 37$ km, are apparently related to changes of structure at faults (see Figure 1). These travel time fluctuations do not prevent analysis of the data by wave field transformation, but as discussed below, they do contribute significantly to the uncertainty associated with the best fit laterally homogeneous model.

Figure 3 shows the slant stack of the data in Figure 2. The desired $p$-$\tau$ locus is an image formed as the envelope of a series of intersecting straight lines. The slope of each line is $-1/x$, where $x$ is the corresponding shot to receiver distance. Where the $t$-$x$ data are not spatially aliased, destructive interference reduces the amplitude contributions off the $p$-$\tau$ locus. Since many of the data traces in Figure 2 are spaced greater than a half wavelength apart, they are spatially aliased, and consequently, many artifical straight lines can be seen throughout Figure 3. As the data traces are unequally spaced, a weighting that depends on trace separation was employed in slant stacking. A fairly coherent image can be seen traversing this wave field in the ($p$, $\tau$) region from (0.188, 0.0) to (0.138, 1.6). The image does have some 'en echelon' branches beside the main locus and some regions where $\tau$ is not monotonically decreasing that are due to the fluctuations in arrival times mentioned above. The consequences of the anomalies can be seen in Figure 4.

Iterative downward continuation of the $p$-$\tau$ wave field in Figure 3 produces the slowness-depth image displayed in Figure 4. The solid line in Figure 4 is the velocity function at the final iteration, and it coincides with the dominant image in

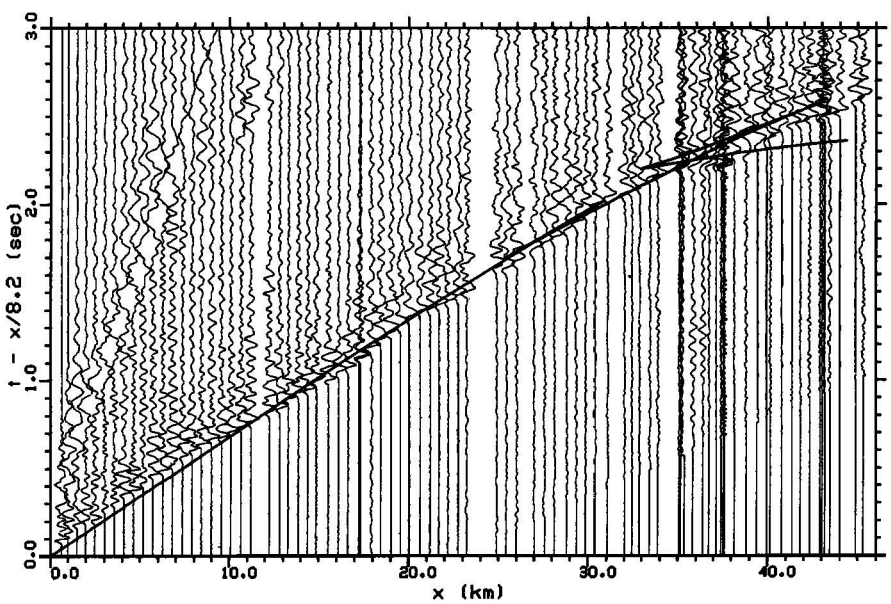


Fig. 7. Comparison of observed travel times with those computed for the unconverged model in Figure 6. The calculated travel times are shown as the solid line.

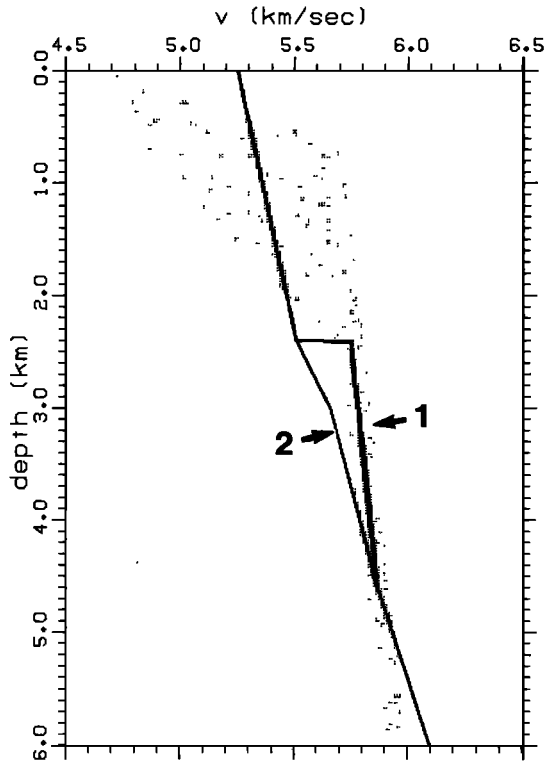


Fig. 8. Comparison of velocity profiles for the Mojave Desert. Model 1 is that in Figure 4, model 2 is that in Figure 6, and the shaded area is an estimate of the range of velocities in this area as obtained independently by two-dimensional ray tracing by *Fuis* [1981].

the downward continued $p$-$z$ wave field. However, because of the lateral variations in structure along the profile, the image is broken and sometimes multivalued. The solid, monotonic velocity-depth curve can therefore be considered only as an average laterally homogeneous approximation to the velocity structure along the profile. The uncertainty in this representation of the structure, which is indicated by the width and incoherence of the image, is $\pm 0.8$ km depth. This uncertainty in depth can be attributed to a composite of two effects. First, the time resolution and frequency content in the original data is seen in the width of the individual branches of the split image, which accounts for about half the variation. The multiplicity of branches due to lateral velocity changes accounts for the remainder.

As a check on the adequacy of the model obtained, travel times were computed for the model by ray tracing. (Note that up to this point, travel times have not been directly used to constrain the model.) The resulting travel time curve is superimposed on the data in Figure 5. In general, the model produces a smooth curve that fits the first arrival observations to within 0.05 s. The fit is early at some distances and late at others, indicating that we have indeed obtained a reasonable average velocity function by downward continuation.

Triplications are evident in the traveltime curve in Figure 5. The one that occurs at 13 km $< x <$ 31 km is due to the rapid velocity increase near 2.3 km depth (Figure 4). This triplication may be real, as there appears to be an increase in waveform complexity near the first arrivals over this distance range, which is consistent with the existence of a triplication. On the other hand, this feature may be an artifact introduced by fortuitous correlations across the variations in first arrival times due to lateral structure changes in this region. The latter interpretation is supported by the absence of the expected precritical reflection image in Figure 4. The precritical reflection would lie horizontal and touch the main image at the depth of the reflector (2.3 km). Examples of precritical reflections are shown in Figure 11 below.

The second triplication lies at $x > 33$ km in Figure 5. This feature is clearly due to lateral rather than vertical velocity variations, as the highest velocity branch results from coherence of energy strongly affected by the San Andreas Fault (near $x = 37$ km). Consequently, the velocities in the model in Figure 4 are not reliable below 6 km depth.

To investigate further the stability of the solution in Figure 4, the model was altered to decrease the velocity gradient near 2.3 km depth. This model is shown as the solid line superimposed on the wave field obtained by downward continuation with it in Figure 6. This model does not give the wave field stationarity required for convergence (note that the shift of the wave field in Figure 6 relative to that in Figure 4); however, as is shown in Figure 7, it fits the observed travel times as well as the convergent model does. To choose between the two models is difficult. The first model has converged, but this is a valid indication of a correct solution primarily for laterally homogeneous media. The second model fits the observed times adequately and is slightly simpler but has not converged. For comparison, Figure 8 shows the two average models discussed here along with a shaded area that corresponds to the estimated range of velocities as determined for the same region by two-dimensional ray tracing [*Fuis*, 1981]. The velocity in the uppermost 2.5 km, which corresponds to fractured granite, is most variable; at these depths our models generally lie within the shaded region. Below 2.5 km the position and velocity gradient of our converged model (curve 1) correspond closely to those of Fuis; those of the smoothed model (curve 2) do not.

In summary, this analysis of the Mojave Desert data illustrates some of the tradeoffs that occur when structure varies

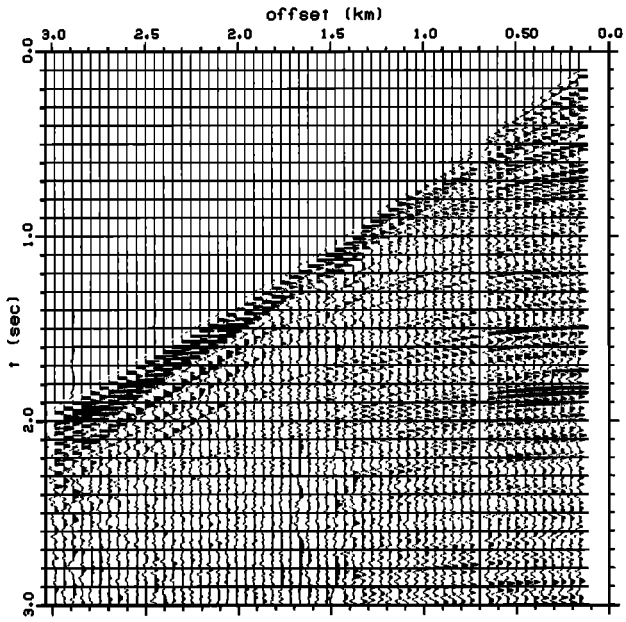


Fig. 9. Common midpoint marine profile. These data are plotted in the reflection seismology convention of time increasing downward (in contrast to the refraction format used for Figure 2). Since this is a common midpoint gather, offset rather than shot distance has been plotted. This example contains prominent precritical reflections that are used as constraints for velocity inversion.

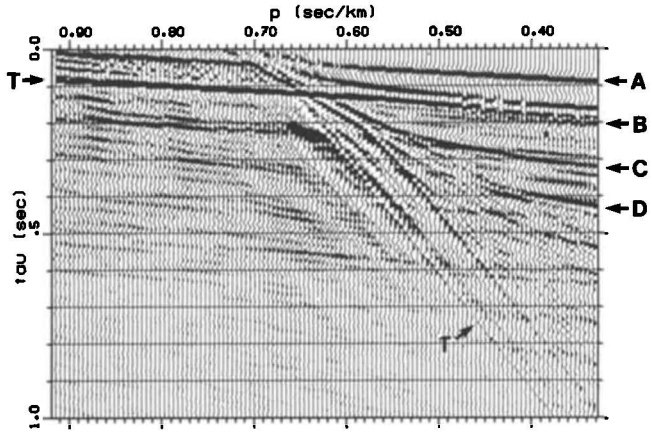


Fig. 10. Slant stack ($p$-$\tau$) wave field obtained by transformation of the marine data in Figure 9. Iterative downward continuation of this $p$-$\tau$ wave field converges with the velocity profile and $p$-$z$ wave field in Figure 11. The curves labeled A through D are precritical reflections. The curves labeled T are cable truncation artifacts.

laterally. Specifically, an equivalent laterally homogeneous velocity-depth curve can be stably estimated, but the finer details of the curve may be related to lateral rather than vertical velocity variation. These effects are not confined to the wave field analysis, but the wave field approach has the advantage of being relatively unbiased as the significance of any region of coherent energy in the data is not established until convergence is obtained. The identification of the possible triplication near 20 km is an example of this.

## A Shallow Marine Profile Containing Precritical Reflections

In a laterally homogeneous region, data in both the common-shot recording geometry and the common midpoint interpretation coordinates used in seismic exploration can be directly inverted by wave field transformation. In this section we present an example of the analysis of a common midpoint gather containing the acoustic response of the uppermost 1 km

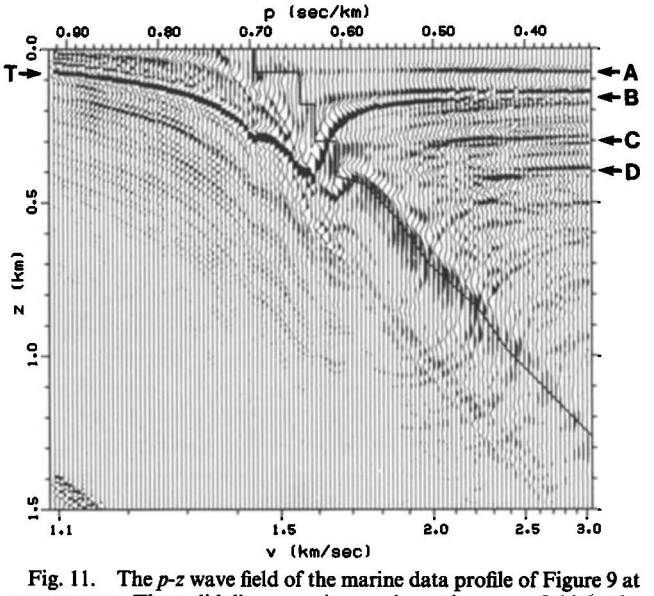


Fig. 11. The $p$-$z$ wave field of the marine data profile of Figure 9 at convergence. The solid line superimposed on the wave field is the velocity-depth function used in the downward continuation. Labeled branches correspond to those labeled in Figures 10, 12, and 13.

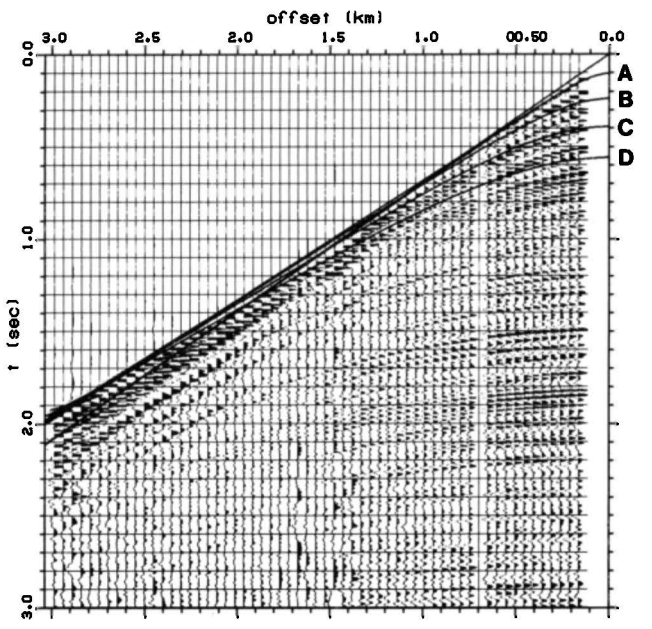


Fig. 12. Comparison of observed and calculated travel times. The solid lines superposed on the data are times predicted from the model in Figure 11. Arrivals are labeled to correspond to those in Figures 10, 11, and 13.

of sediments in a shallow marine environment. The data are shown in Figure 9.

Figure 10 shows the slant stack of the data in Figure 9. There are some artifacts visible in this wave field; the most prominent ones (labeled T in Figure 10) are due to the truncation of the data at the two ends of the recording cable and appear as coherent straight lines. The $p$-$\tau$ image of interest consists of two types of curves. The first is the main trajectory that lies in the ($p$, $\tau$) region from (0.69, 0.0) to (0.45, 0.6). The second type corresponds to precritical reflections which appear as hyperbolic trajectories in the upper right part of Figure 10 (e.g., those labeled A, B, and C).

The strong precritical reflections in these marine data are useful constraints in the downward continuation of the $p$-$\tau$ wavefield to produce the model (the solid line in Figure 11). When the correct velocity function is used, precritical reflec-

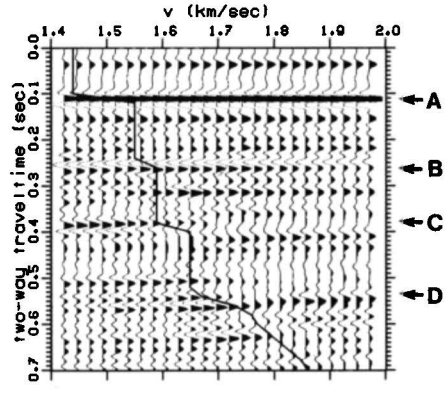


Fig. 13. Overlay of velocity model on data section. The solid curve is the two-way travel time equivalent of the velocity-depth function in Figure 11. The wave field upon which it is plotted is a near-offset reflection section. The first (left) trace is the near-offset trace from the common midpoint data used to derive the velocity profile. The reflections are labeled to correspond to those in Figures 10–12.

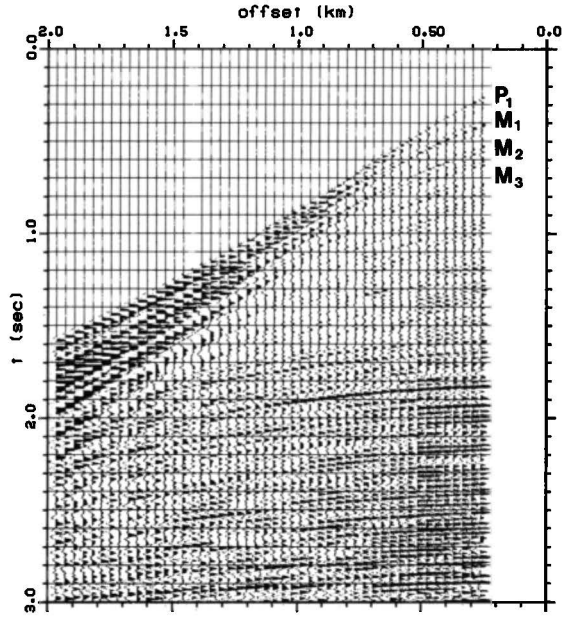


Fig. 14. Common midpoint marine profile. These data contain free-surface water multiples that are used as constraints in velocity inversion. $P_1$ is the primary water bottom reflection, $M_1$ is its first multiple, $M_2$ is its second, and so forth.

tions produce a straight, horizontal image in the $p$-$z$ plane at the depth of the reflector. The image is horizontal because all the $p$ values associated with the reflection event bottom at the same depth. The uppermost reflection (A) in Figure 11 is from the water sediment interface. The image is poorly defined between A and the intersediment reflection B. The rms velocity is, however, apparently correct because image B is straight and horizontal. Similarly, image C corresponds to a reflector at about 0.3 km depth. A major reason that those parts of the image lying between reflections are not well defined is that the cable length is not sufficient to contain all the refracted and postcritical reflection energy. The clearest part of the image is from 0.5 to 1.0 km depth where there is a coherent trajectory, indicating a nearly linear increase of velocity with depth. Such an increase is consistent with the observation of a gently curved first arrival branch in the travel time curve between the 1.5 and 3.0 km offsets in Figure 9. The depth resolution, as defined by the width of the image at convergence, varies from about $\pm 0.03$ km near the surface to about $\pm 0.07$ km near 1.0 km depth.

As a check of the model in Figure 11, the travel times corresponding to this model were computed and superimposed on the data, as shown in Figure 12. In addition to the reflections from the three velocity steps mentioned above, times from the high-velocity gradient near 0.45 km depth (labeled D) is also shown. All four reflections appear to be expressed in the data, particularly at the near offsets. Evidence for additional small velocity steps is seen in the travel time and $p$-$z$ domains. We have attempted to image only the major ones.

Figure 13 contains the superposition of our velocity profile (converted from depth to two-way travel time) upon a near-offset reflection data section. The inversion of the refractions by wave field transformation produced a model whose two-way travel times to the main reflectors that are compatible with those observed in the near-offset section. Velocity increases correspond to the main reflection arrivals in the data.

## A Shallow Marine Profile Containing Water Multiples

Marine data recorded over a hard bottom typically contain prominent multiple reflections whose peglegs are confined to the water column. (Note that these multiples are not the same as the $PP$-type refracted multiples analyzed by *Clayton and McMechan* (1981*b*).) Analysis of such data can be accomplished by imaging the multiples concurrently with the primary energy. The purpose of the following example is to demonstrate concurrent inversion. The acoustic data that are shown in Figure 14 contain at least four water multiples, of which the first two are directly included in the wavefield inversion presented below. The result of this inversion consists of three images of the velocity-depth profile down to 0.6 km depth.

Figure 15 shows the slant stack of the data in Figure 14. In this wave field a number of water multiples (labeled $M$) are visible. The precise location of the primary $p$-$\tau$ locus is not as clear as in the previous examples because of interference between the primaries and multiples, but it is located approximately between ($p$-$\tau$) from (0.67, 0.0) to (0.40, 0.5).

To identify and image the multiples, three $p$-$\tau$ wave fields were concurrently downward continued into $p$-$z$ space. The first of these is the complete $p$-$\tau$ wave field shown in Figure 15. The second is a new $p$-$\tau$ wave field ($p$-$\tau'$) constructed from the first by shifting each $p$ trace toward smaller $\tau$. The amount of shift at each $p$ is equal to the $\tau$ of the primary water bottom reflection of the same $p$:

$$\tau'(p) = \tau(p) - 2\frac{h}{v}(1 - p^2v^2)^{1/2} \tag{3}$$

where $h$ and $v$ are the thickness and velocity of the water layer. Inversion of this modified wave field images the first multiple. Similarly, for imaging the second multiple, another $p$-$\tau$ wave field was constructed by subtracting twice the primary water reflection $\tau$ at each $p$. The result of concurrent imaging of these three $p$-$\tau$ wave fields is the three $p$-$z$ wave fields in Figure 16. The solid line superimposed on all three $p$-$z$ wave fields corresponds to the final $p$-$z$ locus. The uncertainty in this locus is seen to be of the order of $\pm 0.025$ km. In Figure 16*a*, $P_1$ is the precritical primary water bottom reflection and $P_2$ is the precritical primary reflection from a discontinuity near 0.35 km

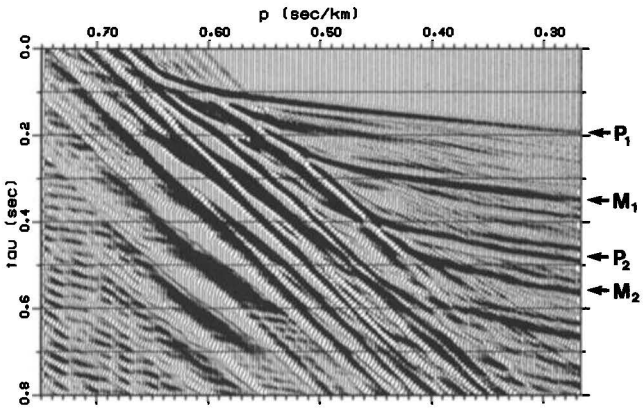


Fig. 15. Slant stack ($p$-$\tau$) wave field obtained by transformation of the marine data in Figure 14. In this wave field a number of water column multiples are present. $P_1$ is the primary water bottom reflection, $M_1$ is its first multiple, $M_2$ is its second, and so forth. $P_2$ is another primary reflection. The imaging of these data produce the $p$-$z$ wave fields in Figure 16.

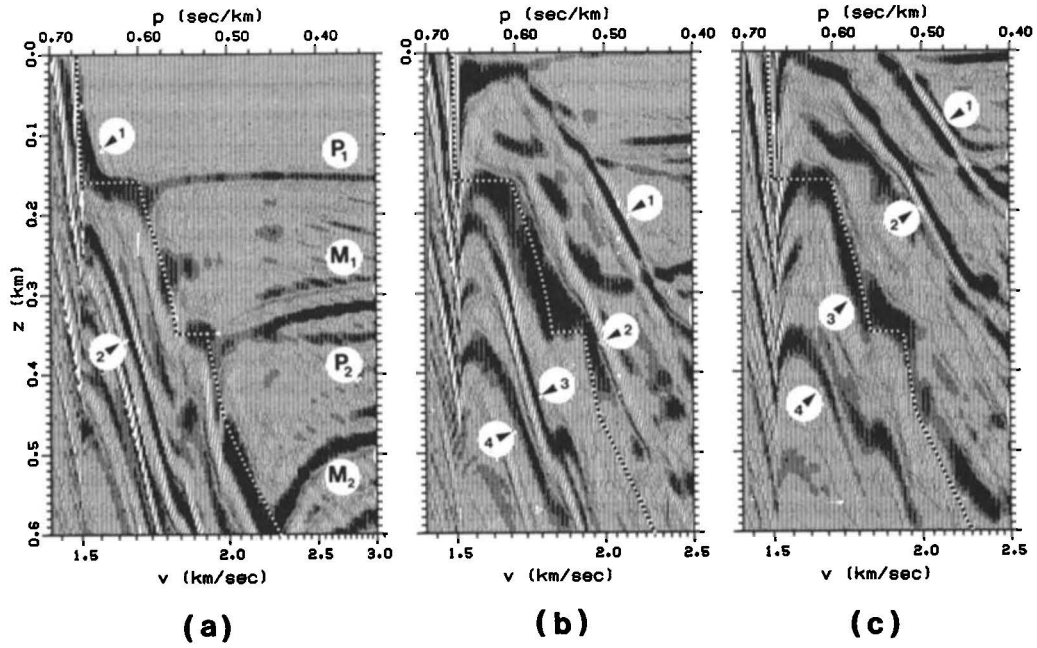


Fig. 16. Concurrent imaging of three $p$-$z$ wave fields. (*a*) The inversion based on the primary energy, (*b*) The first multiple. (*c*) The second multiple. All three image the same $p$-$z$ curve (the dotted line that is superimposed on each). In each panel, the successive images are numbered: 1 for the primary image, 2 for the first multiple image, 3 for the second multiple, and so forth. Branches labeled $M$ and $P$ are precritical reflections disucssed in the text.

depth. Both of these appear horizontal in the $p$-$z$ wave field (Figure 16*a*). The nonhorizontal loci $M_1$ and $M_2$ are the first two water column multiple reflections. In Figure 16*b*, where the $p$-$\tau$ wave field was shifted by $\tau$ corresponding to one water reflection, the primary energy 1 lies above the $p$-$z$ locus 2. In Figure 16*c* where the shift is double, two images (1 and 2) lie above the $p$-$z$ locus 3.

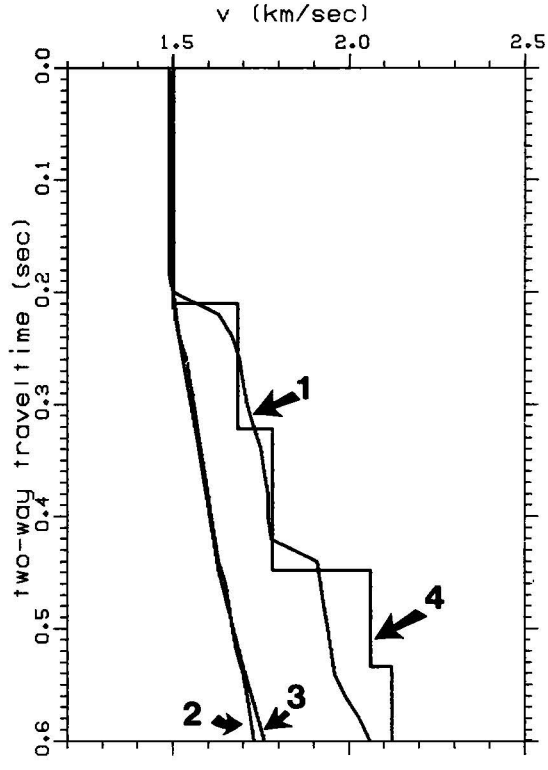


Fig. 17. Comparison of two velocity analyses of the data in Figure 14. Curve 1 is the two-way travel time profile corresponding to the velocity profile plotted in the three panels of Figure 16; 2 is the corresponding rms time profile; 3 is the rms time profile of *Schultz* [1980]; 4 is the time profile corresponding to 3. Curve 1 is to be compared with 4; 2 with 3.

This example illustrates the interpretation problem associated with water multiples. Specifically, precritical multiple reflections cut across the primary branches. This infererence produces an incoherent primary image. When multiples are concurrently inverted with the primary energy, however, a coherent picture emerges as successive multiple loci fill in the ambiguous portions. Figure 17 contains a comparison of our results with those of *Schultz* [1980], who independently analyzed this same data set by a layer-stripping method. Again, the results are compatible with each other.

## Discussion and Summary

One of the advantages of the wave field transformation approach is that no preprocessing of the data is required. The complete data set is used in raw form, so the final image contains no arbitrary selection of data. For analysis of large-scale refraction profiles, such as the Mojave Desert data, wave field transformation produces a solution in a matter of hours. For exploration (reflection) oriented processing, wave field transformation of refractions provides a method of extracting independent velocity information from a portion of the wave field that has previously been neglected by conventional analyses.

The method of refraction inversion by wave field transformation has been illustrated by application to three rather different data sets, one recorded on land in a common shot refraction geometry, and the other two recorded in shallow marine environments with standard acoustic exploration cables. In all three cases, the results obtained are compatible with those of conventional processing. Wave field transformation is seen to be robust, unbiased, and particularly suited to processing large volumes of data. These features, combined with the conceptual elegance involved in forming the solution

from the data itself, encourage further development and application of the method.

*Acknowledgments.* We thank the sponsors of the Stanford Exploration Project for providing financial and computing support, the U. S. Geological Survey for providing the Mojave Desert data, CONOCO for providing the first marine data set, and Digicon for the second. Contribution 950 from the Earth Physics Branch.

## References

Bessonova, E. N., V. M. Fishman, V. Z. Ryaboyi, and G. A. Sitnikova, The tau method for inversion of travel times, 1, Deep seismic sounding data, *Geophys. J. R. Astron. Soc., 36*, 377–398, 1974.

Brocher, T. M., and R. A. Phinney, Inversion of slant stacks using finite-length record sections, *J. Geophys. Res., 86*, 7065–7072, 1981.

Chapman, C. H., A new method for computing synthetic seismograms, *Geophys. J. R. Astron. Soc., 54*, 481–518, 1978.

Chapman, C. H., Generalized radon transform and slant stacks, *Geophys. J. R. Astron. Soc., 66*, 445–453, 1981.

Clayton, R. W., and G. A. McMechan, Inversion of refraction data by wavefield continuation, *Geophysics, 46*, 860–868, 1981*a*.

Clayton, R. W., and G. A. McMechan, Inversion of refracted free-surface multiples by wavefield continuation, submitted to *Geophys. J. R. Astron. Soc.*, 1981*b*.

Fuis, G. S., Crustal structure of the Mojave Desert, *U. S. Geol. Surv. Open File Rep. 81-503*, 36–38, 1981.

McMechan, G. A., and R. Ottolini, Direct observation of a $p$-$\tau$ curve in a slant stacked wavefield, *Bull. Seismol. Soc. Am., 70*, 775–789, 1980.

Schultz, P. S., A method for direct estimation of interval velocities in the near surface, paper presented at the 49th Annual SEG Meeting, Houston, Tex., 1980.

Schultz, P. S., and J. F. Claerbout, Velocity estimation and downward continuation by wave front synthesis, *Geophysics, 43*, 691–714, 1978.

(Received April 15, 1981;
revised October 9, 1981;
accepted October 16, 1981.)